


 Cite this: *RSC Adv.*, 2024, 14, 18385

Exploring half-metallic ferromagnetism and thermoelectric properties of Tl_2WX_6 ($X = Cl$ and Br) double perovskites

 Ghulam M. Mustafa,^a Zaka Ullah,^a M. Adil Ameer,^{a*} N. A. Noor,^b Sohail Mumtaz^c and Mohammad K. Al-Sadoon^d

Half-metallic semiconductors typically exhibit 100% spin polarization at the Fermi level which makes them desired materials for spintronic applications. In this study, we reported a half-metallic ferromagnetic nature in vacancy-ordered double perovskites Tl_2WX_6 ($X = Cl$ and Br). The magnetic, electronic, and thermoelectric properties of the material are studied by the use of density functional theory (DFT). For the calculations of exchange–correlation potential, PBE-sol is employed while more accurate electronic band structure and density of states (DOS) are calculated by the mBJ potential. Both materials exhibited structural stability in the cubic structure with $Fm\bar{3}m$ space-group. The mechanical stability is confirmed by their computed elastic constants while their thermodynamic stability is attested by negative formation energy. The spin-based volume optimization suggested the ferromagnetic nature of the materials which is further confirmed by the negative value of the exchange energy $\Delta_x(pd)$. Moreover, computed magnetic moment value for Tl_2WCl_6 and Tl_2WBr_6 is 2 μ_B and the majority of this comes from W. The spin-polarized band structure and DOS confirmed that both materials are half-metallic and at the Fermi level they exhibit 100% spin polarization. Furthermore, in the spin-down state, materials behave as semiconductors with wide bandgaps. Lastly, the thermoelectric properties are evaluated by the BoltzTrap code. The thermoelectric parameters which include the Seebeck coefficient, electrical conductivity, thermal conductivity, power factor, and figure of merit (ZT) are investigated in the range of temperatures from 200 to 800 K. The half-metallic ferromagnetic and thermoelectric characteristics make these materials desired for spintronics and thermoelectric applications.

 Received 1st April 2024
 Accepted 24th May 2024

DOI: 10.1039/d4ra02465f

rsc.li/rsc-advances

1. Introduction

Spintronics is a growing field of magnetic electronics, that has the potential to revolutionize the world by replacing conventional electronics. In conventional electronics, only the charge of electrons is accounted for while spintronics also utilizes the spin degree of freedom.¹ In 1988, the discovery of giant magnetoresistance (GMR) in multilayer structures consisting of a nonmagnetic conducting layer sandwiched between ferromagnetic magnetic layers provided the foundation for this novel idea of spintronics.² Furthermore, a high tunneling magnetoresistance (TMR) at room temperature was reported in 1995 which makes this phenomenon attractive for the development of magnetic sensors and memory storage devices.³ In

addition, other advanced spin-based devices include spin transistors, spin capacitors, spin valves, and spin lasers.⁴ The advantages of spintronics over conventional electronics are their high-density memory and logic, high speed, and low power consumption⁵ with unlimited endurance.⁶

Spintronics works by creating spin polarization, and materials that provide high spin polarization are considered desirable.⁷ In this regard, several materials which include half metals (HM), ferromagnetic semiconductors (FMS), and dilute magnetic semiconductors (DMS) are considered suitable as HM and FMS provide high spin polarization and DMS provide ease for spin injection.^{8–10} In recent decades, researchers have discovered both half metallic and ferromagnetic characteristics in double perovskite semiconductors (DPs) which make the scientific community to further explore these materials for possible spintronic applications.¹¹ DPs are compounds with the general formula of $ABB'X_6$. Here, A, B, and B' are the cations, where A generally belongs to rare-earth or alkaline earth metals, B and B' are transition metals. In the composition, X represents an anion which may be halogen, oxygen, or chalcogenide.¹² Furthermore, along with their HM and FMS nature, DPs also exhibit optimistic optoelectronic and thermoelectric properties.

^aDepartment of Physics, Division of Science and Technology, University of Education, Lahore, Punjab 54770, Pakistan. E-mail: adilameer7673@gmail.com

^bDepartment of Physics, Riphah International University, Campus Lahore, 53700, Pakistan

^cElectrical and Biological Physics, Kwangwoon University, Seoul, 01897, South Korea

^dDepartment of Zoology, College of Science, King Saud University, P.O. Box 2455, Riyadh 11451, Saudi Arabia



In the context of thermoelectric (TE) properties, DPs possess high electrical and low thermal conductivities,¹³ high thermal stability, and an environment-friendly nature.¹⁴

For spintronic devices to work efficiently at room temperature, those HMs are desired which exhibit a large bandgap to avoid spin flipping of carriers from thermal energy and have a high Curie temperature ($T_c >$ room temperature).¹⁵ In the quest for these properties, Philipp *et al.* reported HM nature in DPs A_2CrWO_6 ($A = Sr, Ca, \text{ and } Ba$). Among these materials, Sr_2CrWO_6 exhibits the highest value of $T_c = 458$ K and it showed a tolerance factor equal to 1 which indicates the undistorted cubic structure. The replacement of Ca and Ba in place of Sr causes a reduction in the value of T_c . Furthermore, partial substitution of La^{2+} in place of Sr^{2+} resulted in the reduction in both saturation magnetization and Curie temperature.¹⁶ In another study, Kumar *et al.* reported a half-metallic ferromagnetic HMFm-DP Ba_2YbTaO_6 , which showed metallic behavior in the spin-down state while exhibiting a wide bandgap of 3.47 eV in the spin-up state.¹⁷ Besides oxide DPs, to explore the HMFm in halide-based DPs, Mir and Gupta studied Cs_2NaMCl_6 ($M = V$ and Ti), and reported the HMFm in both materials with 100% spin polarization. The partial density of states (DOS) plot showed that HMFm properties were contributed by unpaired electrons of split d-orbitals of M-site elements in the crystal field.¹⁸ In context to TE properties, a material with a high figure of merit (ZT) is considered suitable for TE applications. Regarding this, Harbi *et al.* studied Ba_2MWO_6 ($M = Cd, Zn, \text{ and } Mg$) and reported a high figure of merit at 800 K with the values of 0.64, 0.71, and 0.76 for Cd/Zn/Mg compositions respectively. Also, all three materials were found mechanically stable.¹⁹ In a separate study about TE properties Haque and Hossain reported a very low lattice thermal conductivity of $0.2 \text{ W m}^{-1} \text{ K}^{-1}$ for the halide DP $Cs_2InAgCl_6$. By increasing temperature from 300 to 700 K power factor decreases but due to low total thermal conductivity, a high $ZT = 0.74$ was obtained at 700 K.²⁰ Since the process of doping in DPs affects its TE properties, so to investigate these effects, Hira *et al.*, studied $Sr_{2-x}Bi_xCoRuO_6$ ($0 \leq x \leq 0.8$) and reported that with increasing Bi doping, the material changes from n-type to p-type and also a decrease in thermal conductivity was observed. ZT value also increased with increasing Bi content and the highest value of ZT was reported at $x = 0.8$.²¹

Considering these useful properties of DPs reported in the above-mentioned studies, we investigated the structures of vacancy-ordered DPs Tl_2WX_6 ($X = Cl, Br$) along with their mechanical, electronic, magnetic, and thermoelectric properties by using DFT. The reported results of our study are encouraging and are a worthwhile contribution to the existing knowledge of DPs and also showcased the capability of these materials for application in the field of spintronics and thermoelectrics.

2. Computational details

In the present study, we used full potential linearized augmented plane wave (FP-LAPW) calculations for structural optimization and to examine the mechanical, electronic, and

magnetic response of Tl_2WCl/Br_6 . The calculations were performed on the DFT-based Wein2K package. For structural optimization and mechanical properties, exchange correlation potential was evaluated utilizing PBE-sol approximation while for accurate computation of band structure (BS) and density of state (DOS), we utilized mBJ potential. The lattice parameters were calculated by optimization of volume for the lowest ground state energy. To predict the magnetic nature of materials, the volume optimization was implemented separately with initial spin states of antiferromagnetic (AFM) and ferromagnetic (FM) phases. For improved measurements of lattice constants and bulk modulus, the Birch–Murnaghan equation of states was employed.²²

$$E(a) = E_0 + \frac{9B_0V_0}{16} \left[\left\{ \left(\frac{a_0}{a} \right)^2 - 1 \right\}^3 B'_0 + \left\{ \left(\frac{a_0}{a} \right)^2 - 1 \right\}^2 \left\{ 6 - 4 \left(\frac{a_0}{a} \right)^2 \right\} \right] \quad (1)$$

In the above equation, a_0 and V_0 represents the equilibrium lattice constant and volume respectively, E_0 represents energy corresponding to a_0 , B_0 and B'_0 indicates the values of bulk modulus and its derivative with respect to pressure respectively. To evaluate solution of wave function, both muffin tin (MT) and interstitial regions were examined. In the MT region, we assumed a spherically harmonic solution whereas in interstitial regions, plane wave solution of an electronic system was employed. During the whole calculations, we kept some parameters constant. The constant parameters include the value of angular momentum ($l_{\max} = 10$), Gaussian factor $G_{\max} = 20$, and the product of MT radius and wave vector ($R \times K_{\max} = 8$). We select a 2000 k -point mesh as through iteration, we found that the results start to converge at this value of k -points. The energy cutoff was set at 10^{-2} mRy for better convergence. For the computation of thermoelectric properties, semiclassical Boltzmann relations were employed under the fixed relaxation time ($\tau = 10^{-14}$ s). Boltzmann relations were executed by using BoltzTrap code.

3. Results and discussion

3.1. Structural properties

Unlike normal double perovskites, vacancy-ordered double perovskites have a composition of A_2BX_6 in which half of the B site or all the B' site ions are vacant. Fig. 1(a) shows the ball stick model of Tl_2WX_6 ($X = Cl, Br$) in which Tl, W, and Cl/Br ions are represented by grey, pink, and red color balls respectively. It is clear from the figure that W has a 6-fold coordination with Cl/Br while Tl has a 12-fold coordination with Cl/Br. Another structural model is shown in Fig. 1(b), which represents the polyhedral format of compositions. Due to vacancy ordered composition, alternate $B'X_6$ octahedron is not present in the structure leaving behind only the BX_6 or WCl/Br_6 octahedron which is highlighted with grey color. Tl cation exists in the space produced by joined neighboring WCl/Br_6 octahedron. Both of the figures confirm the cubic structure of DPs with the $Fm\bar{3}m$



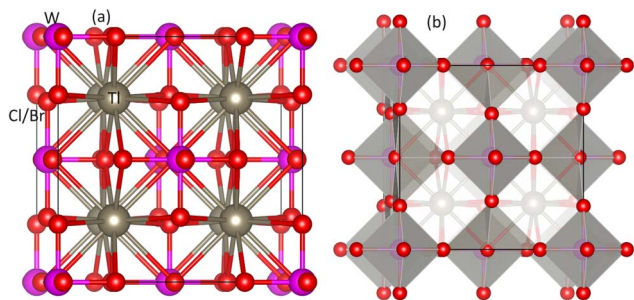


Fig. 1 Unit cell of DPs Tl_2WCl_6/Br_6 (a) ball-stick model and (b) polyhedral model. Tl, W, and Cl/Br ions are represented by gray, pink and red spheres respectively.

space group. The oxidation states of Tl, W, and Cl/Br are +1, +4, and -1 and in both compositions, these ions lie at $8c$, $4a$, and $24e$ Wyckoff positions respectively.

The lattice constants a_0 (Å) were calculated by optimization of unit cell volume of compositions for lowest ground-state energy. Fig. 2 shows the volume optimization against ground state energy and the computed values of lattice constant (a_0) are placed in Table 1. The computed value of a_0 for Tl_2WCl_6 is 9.96 Å which is well matched with the experimental value.²³ It is observed that when Cl is replaced by Br the value of a_0 increases and becomes 10.49 Å. This increase in the value of a_0 resulted because of the larger ionic radius of Br^{-1} as compared to Cl^{-1} . The magnetic ordering was also investigated through volume optimization by separately taking FM and C/G-AFM spin states as initial approximations. Fig. 2(a) and (b) display that optimization of structure was performed for several magnetic conformations, including ferromagnetic (FM), C-type anti-ferromagnetic (C-AFM), and G-type anti-ferromagnetic (G-AFM). It was found that both DPs phases were stable in ferromagnetic phase. This shows that ferromagnetic ordering is dynamically promising for these states, proposing a particular magnetic configuration that improves their stability. Moreover, energies of formation ΔH_f were calculated to examine thermodynamic stability. ΔH_f was given by difference of total energy of a compound and sum of energies of individual elements. The

Table 1 The optimized lattice constants (a_0), bulk modulus (B_0), the ground-state energy differences between AFM and FM phases, Curie temperature (T_c (K)) and formation energy (ΔH_f (eV)) of DPs Tl_2WCl_6/Br_6

| DPs | a_0 (Å) | B_0 (GPa) | $\Delta E = E_{AFM} - E_{FM}$ | T_c | ΔH_f |
|-------------|----------------|-------------|-------------------------------|-------|--------------|
| Tl_2WCl_6 | 9.96 | 46.25 | 19.21 | 558 | -1.38 |
| Exp. | 9.87 (ref. 23) | | | | |
| Tl_2WBr_6 | 10.49 | 37.50 | 11.06 | 524 | -1.04 |
| Exp. | — | | | | |

formation energy values are presented in Table 1, which are -1.38 eV and -1.04 eV for the Cl and Br based composition respectively. A negative sign shows that the energy is released during formation which testify to the thermodynamic stability of the compositions. Since the unit cell of Tl_2WCl_6 releases more energy during formation than Tl_2WBr_6 , so the former composition is more stable.

3.2. Mechanical properties

The mechanical stability of the materials was tested by estimating their elastic stiffness constants. Elastic constants help to understand the behavior of materials toward stress. For cubic crystal structure, there are 3 elastic stiffness constants which are C_{11} , C_{12} , and C_{44} . The calculated values of these stiffness constants are listed in Table 2. The mechanical stability of a cubic structure is described by Born stability criteria which states that a cubic structure is stable if $C_{11} - C_{12}$, $C_{11} - 2C_{12}$, and C_{44} must be greater than zero.²⁴ The calculated constants satisfy these conditions and hence the materials are mechanically stable. Moreover, elastic moduli which include shear modulus

Table 2 The computed values of elastic constants (C_{11} , C_{12} , C_{44}), elastic moduli (B_0 , G and Y), B_0/G , ν and anisotropy (A)

| DPs | C_{11} | C_{12} | C_{44} | B_0 | G | Y | B_0/G | ν | A |
|-------------|----------|----------|----------|-------|-------|-------|---------|-------|------|
| Tl_2WCl_6 | 95.55 | 20.49 | 13.38 | 45.51 | 20.52 | 53.53 | 2.22 | 0.30 | 0.36 |
| Tl_2WBr_6 | 82.09 | 14.90 | 12.69 | 37.29 | 18.97 | 48.66 | 1.96 | 0.28 | 0.37 |

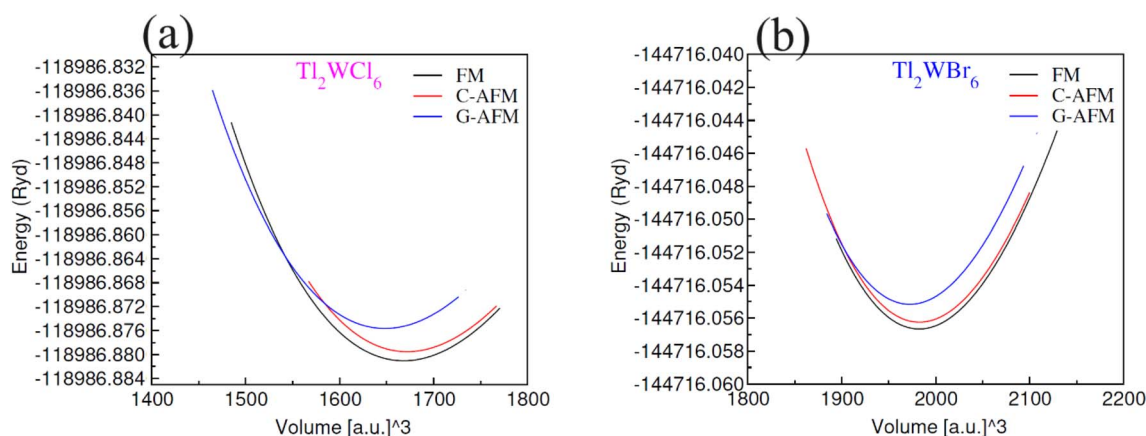


Fig. 2 Plots of volume optimization for DPs (a) Tl_2WCl_6 and (b) Tl_2WBr_6 in FM, C-AFM and G-AFM phases.



(G), bulk modulus (B_0) and young modulus (Y), were calculated and enlisted in Table 2. It is observed that the values of stiffness constants and elastic moduli are greater in case of Tl_2WCl_6 which means that it is more rigid as compared to Tl_2WBr_6 . The behavior of a decrease in the elastic moduli and elastic stiffness constants, when Cl is replaced by Br, is because of the increase in lattice constants.²⁵ Furthermore, in order to check whether the materials are ductile or brittle, Poisson (ν) and Pugh (B_0/G) ratios were computed. A material is considered ductile if $\nu > 0.26$ and $B_0/G > 1.75$.^{26,27} The calculated values of ν and B_0/G show that both materials are ductile in nature. A ductile or brittle nature can also be confirmed by the term $C_{12}-C_{44}$ called Cauchy pressure. If the Cauchy pressure is positive then material is ductile and it is brittle in case of a negative value.²⁸ The positive magnitude of $C_{12}-C_{44}$ confirmed the ductile nature of both compositions. The values of ν , B_0/G , and A are written in Table 2. The anisotropic properties of a material can be evaluated using the formula;

$$A = \frac{2C_{44}}{C_{11} - C_{12}}$$

In an ideal isotropic system, the value of A is one. However, any deviation from this value indicates anisotropic behavior. For the compounds Tl_2WCl/Br_6 , the calculated A values are 0.36 and 0.37, respectively, demonstrating the anisotropic nature of these materials as shown in Table 2.

3.3. Electronic properties

The electronic conduction mechanism can be understood by investigating electronic band structure. The band structure was examined through a band structure diagram which is presented in Fig. 3. The band structure diagram of materials was obtained in energy ranges from -6 eV to $+6$ eV. The spin-polarized band structure confirmed that both materials are halfmetallic in nature. The materials show metallic behavior in up-spin

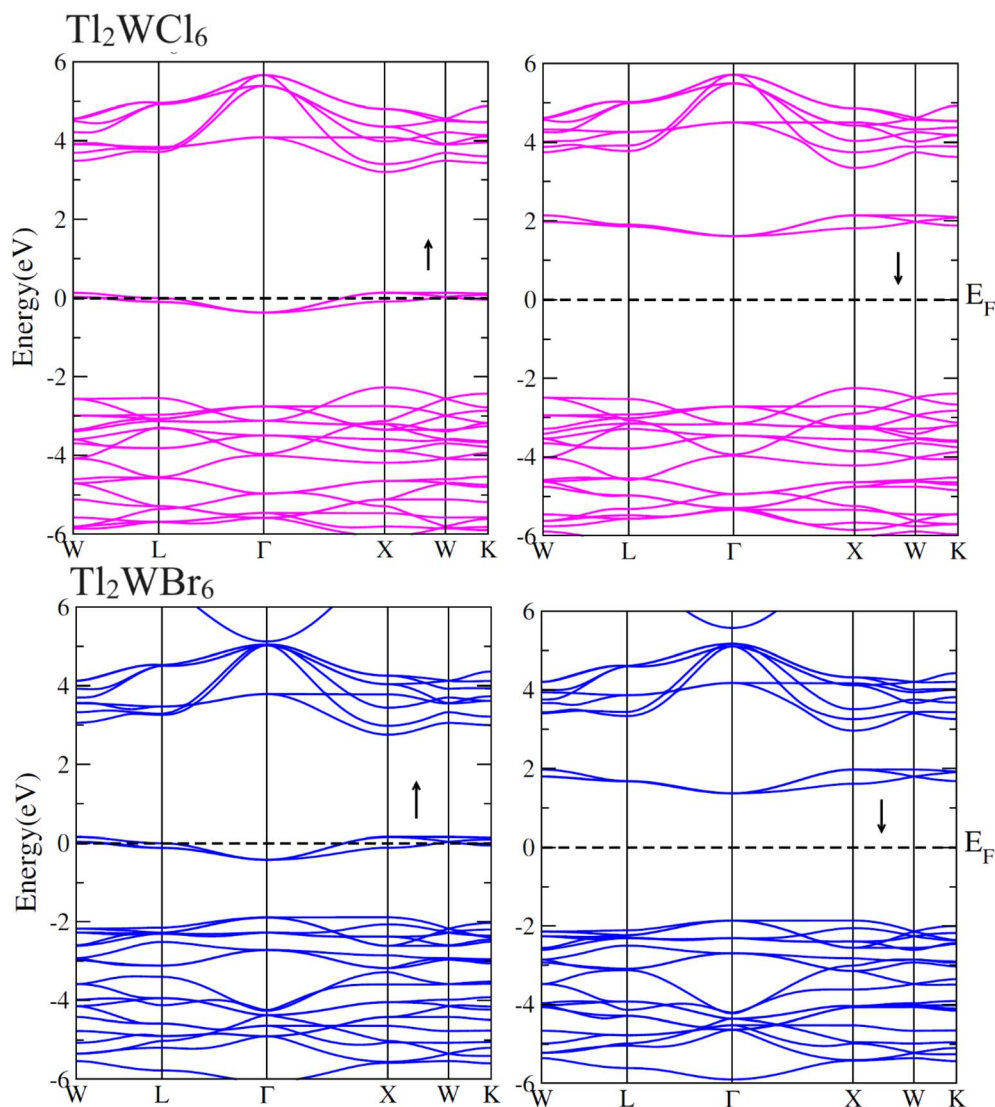


Fig. 3 Calculated band structures for DPs $Cs_2W(Cl/Br)_6$ in spin-up (\uparrow) and spin-down (\downarrow) by utilizing mBJ potential.



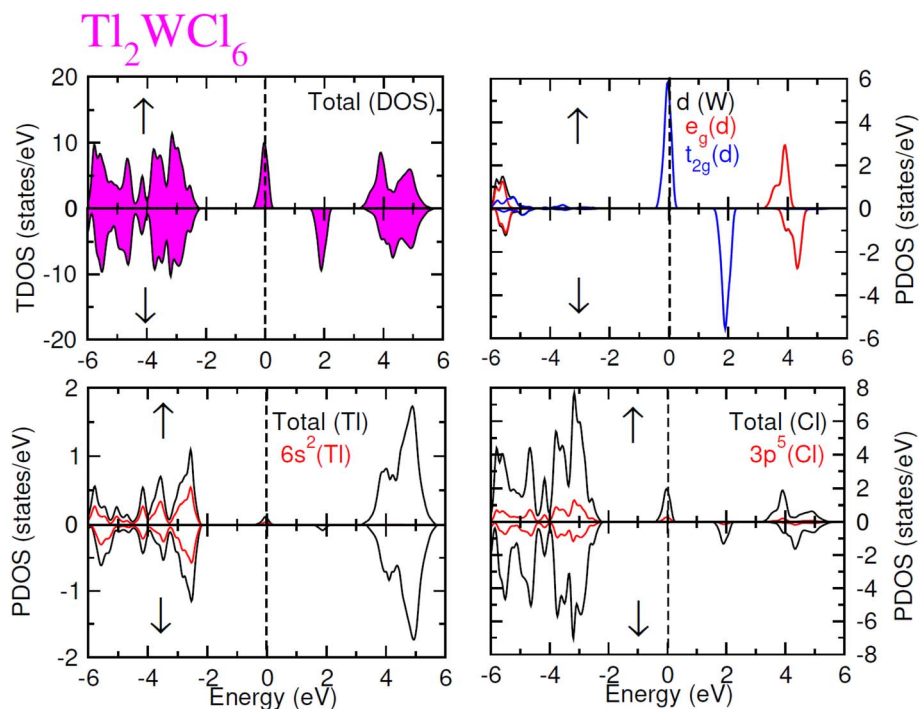


Fig. 4 Total DOS and partial DOS for DP Ti_2WCl_6 and Ti, W and Cl ions in spin-up (\uparrow) and spin-down (\downarrow) channels by utilizing mBJ potential.

configuration whereas in down-spin configuration, Fermi level lies between the conduction band (CB) and valence band (VB) which shows that in this spin state, the materials are semiconductors. Moreover, the materials exhibit wide bandgaps (E_g) as shown in Fig. 3. In the case of Ti_2WCl_6 , the E_g is indirect because the VB maxima and CB minima lie at different K-

points. The VB maxima lie at the X-symmetry point while the CB minima lie at the Γ -symmetry point. Whereas, Ti_2WBr_6 exhibits a direct bandgap because the energy maxima of VB and energy minima of CB lie at the same Γ -symmetry point. In order to further understand band structure and contribution of different electronic states in the HM nature of materials, total

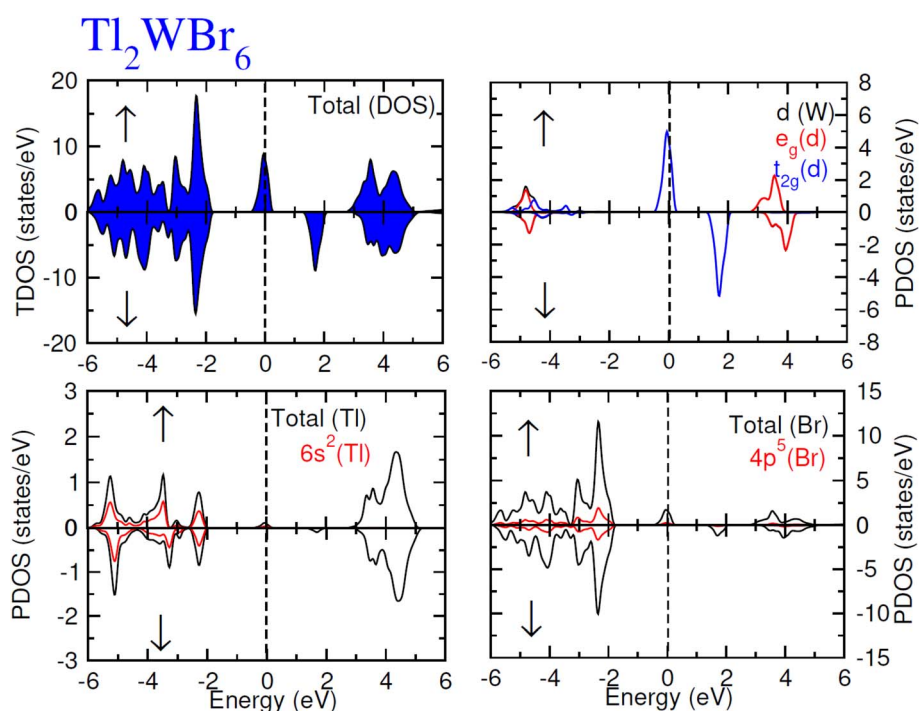


Fig. 5 Total DOS and partial DOS for DP Ti_2WBr_6 and Ti, W and Br ions in spin-up (\uparrow) and spin-down (\downarrow) channels by utilizing mBJ potential.



density of states (TDOS) and partial density of states (PDOS) were examined in the same energy range as in the band structure diagram, and their plots are presented in Fig. 4 and 5. TDOS of Tl_2WCl_6 and Tl_2WBr_6 as shown in Fig. 4 and 5 in up-spin shows non-zero DOS at the Fermi level which continuously spread across Fermi level demonstrating metallic character while in down-spin, it shows a wide bandgap. HMs are the compounds that generally possess 100% spin polarization which can be computed utilizing given relation:

$$P = \frac{N\uparrow - N\downarrow}{N\uparrow + N\downarrow} \times 100\% \quad (2)$$

Here, $N\uparrow$ and $N\downarrow$ show the DOS at the Fermi level in spin-up and spin-down respectively.²⁹ According to the above relation, studied materials exhibit 100% spin polarization at Fermi level. In Fig. 4, PDOS plots of Tl_2WCl_6 show that in this composition, metallic behavior in spin-up is because of major contribution of d- t_{2g} states of W and a minor contribution by the electronic states of Tl and Cl. In spin-down, where the E_g is present, near the Fermi level, the VB is formed by the major contribution of states of Cl and then Tl and with a very little contribution of d- t_{2g} states of W. In the formation of CB, d- t_{2g} has a vital role while there is a small role of Cl and Tl's states. In the case of Tl_2WBr_6 , its PDOS illustrated in Fig. 5, shows that d- t_{2g} states of W and electronic states of Br are responsible for metallic behavior in spin-up, with an insignificant contribution of Tl's state also. In spin-down, near Fermi level, VB is formed by a vital role of Br states and a small share of states of Tl while the edges of the CB are majorly shaped by d- t_{2g} states of W with a meager and negligible contribution of electronic states of Br and Tl respectively.

3.4. Magnetic properties

To examine the magnetic characteristics of materials, exchange mechanism is crucial to understand. The parameters which are related to the exchange mechanism include crystal field splitting (Δ_{CF}), exchange splitting ($\Delta_x(d)$), and indirect exchange energy $\Delta_x(pd)$. The Δ_{CF} arises from the splitting of degenerated d-orbitals of W. When six Cl/Br ligands surround the W cation in an octahedral manner then due to the non-spherical field of ligands, the d-orbitals of W split into three low-energy degenerated t_{2g} orbitals while two high-energy degenerated e_g orbitals. Δ_{CF} is the difference of energy between these e_g and t_{2g} orbitals.³⁰ On the other hand, $\Delta_x(d)$ can be calculated by the difference of energy among corresponding up-spin and down-spin peaks of d-orbitals.³¹ The values of Δ_{CF} and $\Delta_x(d)$ are tabulated in Table 3. It can be seen from the results that $\Delta_x(d) < \Delta_{CF}$, and this shows that ferromagnetic nature is dominated in both compositions. The third

parameter $\Delta_x(pd)$ (which arises from d-states of W and p-states of Cl/Br) can be calculated by taking the difference of energy of valence band maxima in down-spin and up-spin states.³²

$$\Delta_x(pd) = E_v^\downarrow - E_v^\uparrow \quad (3)$$

Here, E_v^\downarrow and E_v^\uparrow are the energy of VB maxima in down-spin (\downarrow) and up-spin (\uparrow) respectively. According to the definition of $\Delta_x(pd)$, a negative value signifies that the energy of the spin-down state is lower, indicating a preference for downward spin orientation. In ferromagnetism, this preference leads to the alignment of magnetic moments in the same direction, contributing to the overall magnetization of the material.³³ The values of $\Delta_x(pd)$ is listed in Table 3. For further examination of magnetic properties, we calculated s-d and p-d exchange constants $N_o\alpha$ and $N_o\beta$ respectively from the difference of energy between down and up-spin states. This energy difference arises from edge splitting at CB minima ($\Delta E_c = E_c^\downarrow - E_c^\uparrow$) and VB maxima ($\Delta E_v = E_v^\downarrow - E_v^\uparrow$). The following relations are used for calculations of these constants.

$$N_o\alpha = \frac{\Delta E_c}{x\langle S \rangle}; N_o\beta = \frac{\Delta E_v}{x\langle S \rangle} \quad (4)$$

Here, x represents the magnetic ion's concentration while S represents the mean value of magnetic moment of a magnetic ion. The value of these exchange constants is written in Table 3. The positive magnitude of $N_o\alpha$ and negative magnitude of $N_o\beta$ are obtained which is a typical response in HMFM semiconductors.³³

The total magnetic moment along with local magnetic moment of Tl, W and Cl/Br were calculated and enlisted in Table 4. It is observed that both compositions have the same value for total magnetic moment with a major contribution from W ions while Tl and Cl/Br contribute insignificantly to net magnetic moment. Since the magnetic moment in an energy range arises from spin polarization which depends on the difference of integral of spin DOS in that range of energy, so, the exchange splitting induces magnetic moment. The large exchange splitting in d-orbitals of W is accountable for its larger magnetic moment as this makes one spin state favorable below the Fermi level. Moreover, the interstitial magnetic moment was also calculated and it has a decent share in the net magnetic moment. The interstitial magnetic moment values are given in Table 4. Since for spintronic devices to work at room temperature, their Curie temperature (T_c) must be higher than room temperature. The Curie temperature (T_c) has been computed by utilizing smearing in mean-field approximations, stated as

$$k_B T_c = \frac{2}{3} \Delta E. \quad (5)$$

Table 3 The estimated magnitudes of Δ_{CF} , $\Delta_x(d)$, $\Delta_x(pd)$, $N_o\alpha$ and $N_o\beta$ for DPs Tl_2WCl_6/Br_6

| DPs | Δ_{CF} | $\Delta_x(d)$ | $\Delta_x(pd)$ | $N_o\alpha$ | $N_o\beta$ |
|-------------|---------------|---------------|----------------|-------------|------------|
| Tl_2WCl_6 | 5.8 | 4.2 | -2.2 | 0.42 | -2.93 |
| Tl_2WBr_6 | 5.4 | 3.9 | -1.9 | 0.31 | -2.56 |

Table 4 Magnetic moments value for DPs Tl_2WCl_6/Br_6 , total and their local M_{Tl} , M_W , and $M_{Cl/Br}$, interstitial ($M_{Int.}$)

| DPs | M_{Total} | $M_{Int.}$ | M_{Tl} | M_W | $M_{Cl/Br}$ |
|-------------|-------------|------------|----------|-------|-------------|
| Tl_2WCl_6 | 2.000 | 0.451 | 0.001 | 1.488 | 0.009 |
| Tl_2WBr_6 | 2.000 | 0.487 | 0.002 | 1.481 | 0.004 |



atoms is described as difference of energy between FM and AFM states $\Delta E = E_{\text{FM}} - E_{\text{AFM}}$. The calculated values of T_c for studied materials were obtained very large as compared to room temperature. The T_c values are given in Table 1 as 558 and 524 K for Ti_2WCl_6 and Ti_2WBr_6 respectively. The HMFM nature of these materials with a wide E_g in minority spin channels and larger T_c make them potential candidates for practical spintronic applications.

3.5. Thermoelectric properties

All the energy generation processes are not 100% efficient and a great amount of energy in the form of heat is wasted in the environment. In this situation, thermoelectric (TE) devices provide an eco-friendly way to convert this wasted heat into electrical energy. In recent decades, materials that possess TE characteristics have been studied extensively. In this article, we reported TE properties of Ti_2WCl_6 and Ti_2WBr_6 calculated by the BoltzTrap code. The reported TE properties include Seebeck coefficient S , thermal and electrical conductivities per relaxation time (κ_e/τ) and (σ/τ) respectively, magnetic susceptibility (χ), power factor (P.F.), and figure of merit (ZT) in the range of temperature from 200–800 K. Due to its half-metallic nature,

these parameters give different results in different spin channels, so the net effect of these parameters can be calculated using following expressions.³⁴

$$\sigma = \frac{\sigma(\uparrow) + \sigma(\downarrow)}{2} \quad (5)$$

$$\kappa = \frac{\kappa(\uparrow) + \kappa(\downarrow)}{2} \quad (6)$$

$$S = \frac{\sigma(\uparrow)S(\uparrow) + \sigma(\downarrow)S(\downarrow)}{\sigma(\uparrow) + \sigma(\downarrow)} \quad (7)$$

In Fig. 6(a), (σ/τ) for both compositions are observed to decrease with an increase in temperature. At 200 K their values are 2.45×10^{19} and $2.6 \times 10^{19} (\Omega \text{ ms})^{-1}$ for Cl and Br-based composition which decreases with temperature and becomes 1.8×10^{19} and $2.13 \times 10^{19} (\Omega \text{ ms})^{-1}$ at 800 K respectively. The decrease in the (σ/τ) arises because of the HM nature of materials with wide E_g as (σ/τ) in spin-up decreases due to metallic nature in that spin channel while in spin-down, owing to wide E_g , the carrier density cannot increase significantly causing net (σ/τ) to decrease. The total thermal conductivity (κ) is the sum of

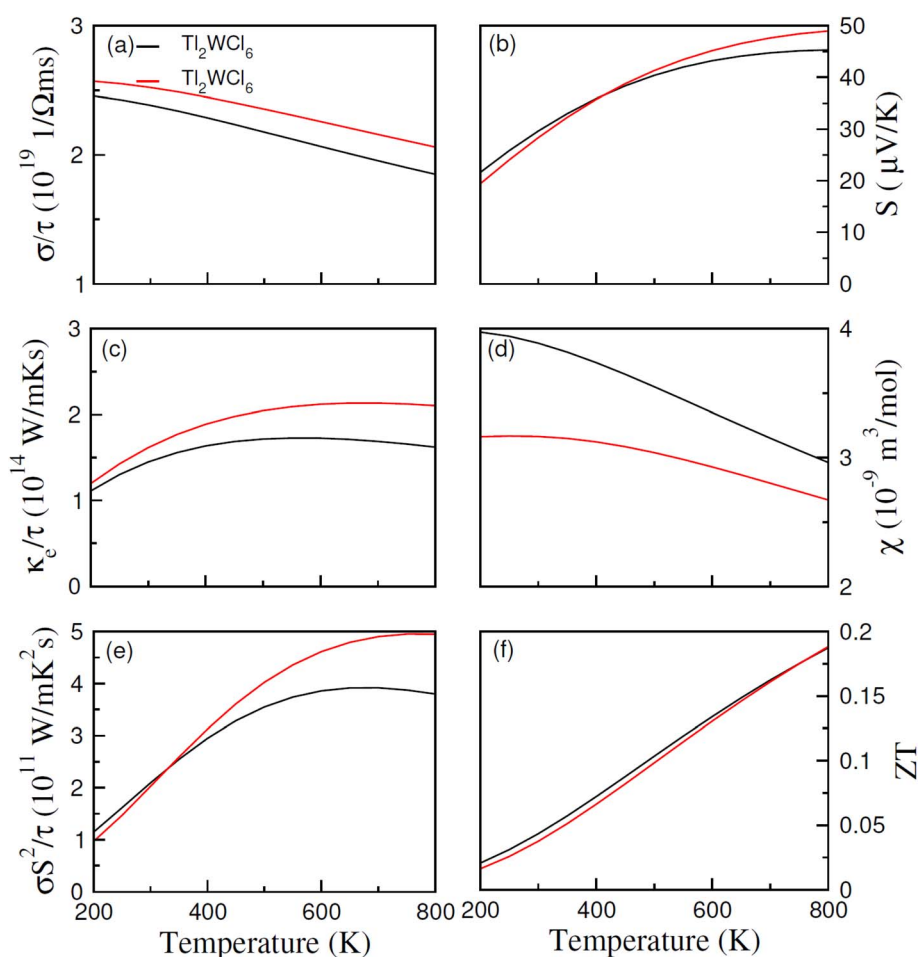


Fig. 6 The calculated values of (a) σ/τ , (b) S , (c) κ_e/τ , (d) χ , (e) power factor and (f) ZT against temperature for DPs $\text{Ti}_2\text{W}(\text{Cl}/\text{Br})_6$ using BoltzTrap code.



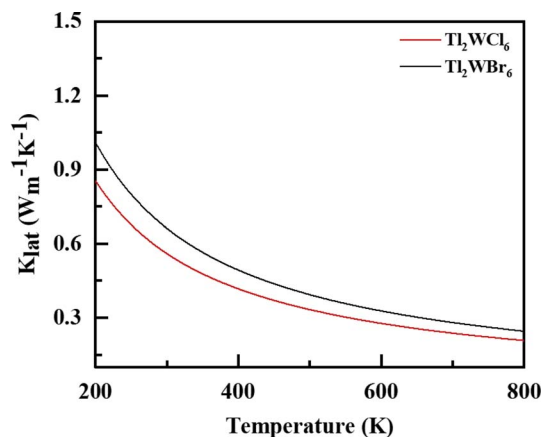


Fig. 7 The calculated lattice conductivity (k_{lat}/τ) for DPs $\text{Tl}_2\text{W}(\text{Cl}/\text{Br})_6$ against temperature 200–800 K.

thermal conductivity contributed by charge carriers (κ_e) and lattice vibrations or phonons (κ_L). In this work, we only computed κ_e , and their values were displayed in Fig. 6(c). At 200 K, Tl_2WCl_6 and Tl_2WBr_6 have the (κ_e/τ) of 1.1×10^{14} and $1.2 \times 10^{14} \text{ W m K}^{-1} \text{ s}^{-1}$ respectively which first increases non-linearly with temperature and then start to decrease and gives the final values of 1.65×10^{14} and $2.15 \times 10^{14} \text{ W m K}^{-1} \text{ s}^{-1}$ at 800 K respectively for Tl_2WCl_6 and Tl_2WBr_6 . The ratio (κ_e/σ) is found to be in the order of 10^{-5} making it a suitable candidate for TE applications. Another important parameter is Seebeck coefficient (S) which measures magnitude of potential difference induced at the ends of TE material when it is subjected to temperature gradient. The magnitude of S can be estimated by using the Pisarenko relation.³⁵

$$S = \frac{8\pi^2 k_B^2}{3eh^2} m^* T \left(\frac{\pi}{3n} \right)^{\frac{2}{3}} \quad (8)$$

Here, the symbols e , h , k_B , T , m^* , and n represent the carrier's charge, Planck's constant, Boltzmann constant, the absolute value of temperature, effective mass of charge carrier, and carrier concentration respectively.

It is observed from Fig. 6(b), that S increases for both materials when temperature is increased. The estimated values of S at 200 K are 19.5 and 21.5 $\mu\text{V K}^{-1}$, which at 800 K becomes 45 and 49 $\mu\text{V K}^{-1}$ for Tl_2WCl_6 and Tl_2WBr_6 . This increasing behavior is because of the direct relation between S and T . Moreover, positive magnitude of S shows majority of positive charge carriers. To analyze effect of temperature on the magnetization of the materials, their magnetic susceptibility (χ) against temperature range of 200–800 K was calculated and presented in Fig. 6(d). Magnetic susceptibility is the measure of the magnetization of materials in the existence of applied magnetic field. It is noted from figure that χ decreases by increasing temperature which is a typical response in the case of ferromagnetic materials and follows the Curie Weiss law. When temperature increases, the thermal energy disrupts the alignment of domains, which causes a decrease in magnetization which in turn decreases the χ . In order to probe how efficiently, a TE material works and convert thermal energy into electrical energy, a parameter named power factor (P.F.) was calculated. The power factor was calculated by the relation $\text{P.F.} = \sigma S^2/\tau$ and its values are demonstrated in Fig. 6(e). At 200 K, P.F. value is 1.2×10^{11} and $1.0 \times 10^{11} \text{ W m K}^{-2} \text{ s}^{-1}$ for Tl_2WCl_6 and Tl_2WBr_6 respectively. An increasing trend is observed in the P.F. for both materials and at 800 K it becomes $3.7 \times 10^{11} \text{ W m K}^{-2} \text{ s}^{-1}$ for Cl-based material and $5 \times 10^{11} \text{ W m K}^{-2} \text{ s}^{-1}$ for Br-based material. Lastly, the overall performance of any TE material can be assessed by an ultimate dimensionless quantity called figure of merit (ZT). The ZT value can be measured using the relation $ZT = (S^2\sigma/\kappa)T$ and its computed values are illustrated in Fig. 6(f). In the case of Tl_2WCl_6 , at 200 K the computed ZT is 0.02 which increases almost linearly and becomes 0.185 at 800 K while in the case of Tl_2WBr_6 , the value of ZT is 0.016 and 0.185 at 200 K and 800 K respectively.

To accurately determine the actual values of ZT , it is essential to explain lattice thermal conductivity (κ_L). Therefore, κ_L is computed separately and shown in Fig. 7 as a function of temperature (T).³⁶ The low κ_L values for both compositions indicate that its contribution is minimal, which is advantageous for enhancing the performance of these materials. Specifically,

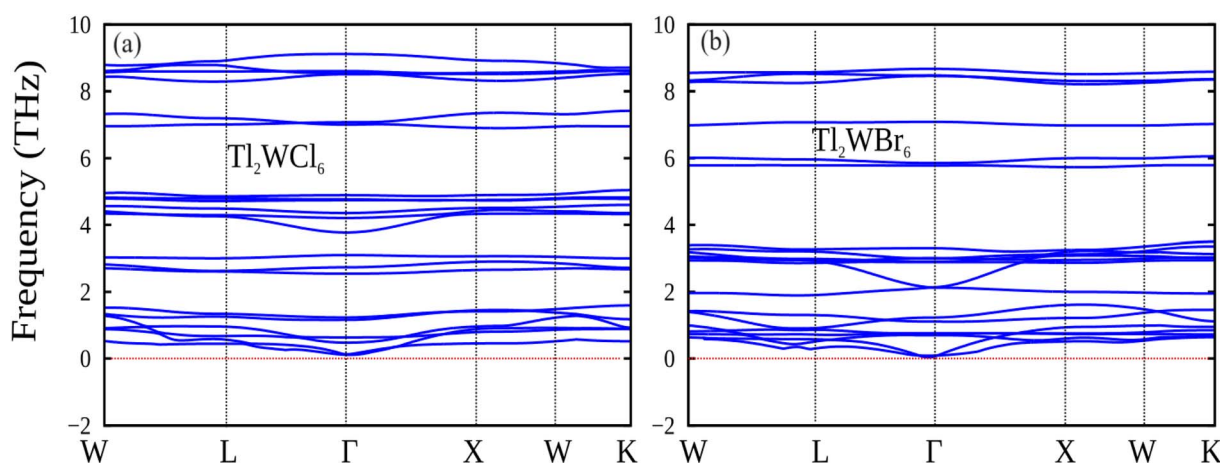


Fig. 8 The calculated phonon dispersion plot for DPs (a) Tl_2WCl_6 and (b) Tl_2WBr_6 .



the κ_L value for Tl_2WCl_6 is reported as 0.85 and for Tl_2WBr_6 is 1.03 W m K^{-1} at 200 K. These values decrease to 0.21 and 0.27 W m K^{-1} at 800 K, respectively, highlighting the significant contribution of κ_L to the overall value of thermal conductivity of these materials.³⁷

3.6. Phonon dispersion plot

Fig. 8 presents the phonon band spectra for the double perovskites Tl_2WX_6 ($X = \text{Cl}$ and Br), which is computed using the PBE-GGA approximation.³⁸ Each double perovskite structure, comprising 9 atoms, yields a total of 27 phonon modes. These modes are categorized into 3 acoustic and 24 optical phonons. The positive frequency values confirm the stability of the studied double perovskite compositions.³⁹

4. Conclusion

In this study, we comprehensively explored DPs Tl_2WX_6 ($X = \text{Cl}$ and Br) for their electronic, magnetic, and thermoelectric properties by utilizing DFT. The materials were found to be mechanically stable and ductile as suggested by their computed elastic constants. The negative formation energies (ΔH_f) testify that both materials were thermodynamically stable. The values of ΔH_f for Tl_2WCl_6 and Tl_2WBr_6 were -1.38 and -1.04 eV respectively, which indicates that the former one is more stable with more energy released at the time of formation. Volume optimization showed that materials with ferromagnetic spin states have the lowest energies which indicated that they are more stable in the ferromagnetic phase than the antiferromagnetic phase. The band structure diagram and DOS depicted that the materials are half-metallic and at Fermi level they exhibited 100% spin polarization. Both compositions exhibited metallic character in up-spin configuration and a wide bandgap in down-spin states. Moreover, (+ve) values of $N_o\alpha$ and (–ve) values of $N_o\beta$ give further evidence of halfmetallic ferromagnetic nature. Moreover, a high T_c for Tl_2WCl_6 and Tl_2WBr_6 was obtained with values of 558 and 524 K which are well above the room temperature. In regards to thermoelectric (TE) properties, electrical conductivity (σ/τ), and magnetic susceptibility (χ) were found to decrease with temperature while other TE parameters which include, Seebeck coefficient (S), electronic part of thermal conductivity (k_e/τ), power factor (P.F.), and figure of merit (ZT) increases with temperature. The calculated ZT for both materials were 0.185 at 800 K. The halfmetallic ferromagnetism with a high curie temperature and wide bandgap along with TE characteristics make these materials potential candidates for spintronic and TE applications.

Conflicts of interest

There are no conflicts to declare.

Acknowledgements

We extend our appreciation to the Researchers Supporting Project (RSP2024R410), King Saud University, Riyadh, Saudi Arabia.

References

- 1 B. Diény, I. L. Prejbeanu, K. Garello, P. Gambardella, P. Freitas, R. Lehndorff, P. Bortolotti, *et al.*, *Nat. Electron.*, 2020, **3**(8), 446–459.
- 2 A. Fert, *Rev. Mod. Phys.*, 2008, **80**(4), 1517.
- 3 J. R. Childress and R. E. Fontana Jr, *Compt. Rendus Phys.*, 2005, **6**(9), 997–1012.
- 4 A. Hirohata and K. Takanashi, *J. Phys. D: Appl. Phys.*, 2014, **47**(19), 193001.
- 5 A. Hirohata, K. Yamada, Y. Nakatani, I. L. Prejbeanu, B. Diény, P. Pirro and B. Hillebrands, *J. Magn. Magn. Mater.*, 2020, **509**, 166711.
- 6 W. Kang, Y. Zhang, Z. Wang, J. O. Klein, C. Chappert, D. Ravelosona, W. Zhao, *et al.*, *ACM J. Emerg. Technol. Comput. Syst.*, 2015, **12**(2), 1–42.
- 7 K. Inomata, N. Ikeda, N. Tezuka, R. Goto, S. Sugimoto, M. Wojcik and E. Jedryka, *Sci. Technol. Adv. Mater.*, 2008, **9**(1), 014101.
- 8 M. Fonin, Y. Dedkov, C. König, G. Güntherodt, U. Rüdiger, J. Mayer, S. Molodtsov, *et al.*, *Adv. Solid State Phys.*, 2003, 487–504.
- 9 Y. Guo, Y. Zhang, S. Yuan, B. Wang and J. Wang, *Nanoscale*, 2018, **10**(37), 18036–18042.
- 10 G. Schmidt and L. W. Molenkamp, *J. Appl. Phys.*, 2001, **89**(11), 7443–7447.
- 11 Y. Zhang and V. Ji, *J. Phys. Chem. Solids*, 2012, **73**(9), 1116–1121.
- 12 R. Chaurasiya, S. Auluck and A. Dixit, *Comput. Condens. Matter*, 2018, **14**, 27–35.
- 13 S. K. Singh, J. A. Abraham, A. S. Alofi, A. Srivastava, K. L. Meena, B. Alshahrani, A. J. A. Moayad, *et al.*, *RSC Adv.*, 2023, **13**(50), 35145–35160.
- 14 T. Maiti, M. Saxena and P. Roy, *J. Mater. Res.*, 2019, **34**(1), 107–125.
- 15 X. Li and J. Yang, *Comput. Mol. Sci.*, 2017, **7**(4), e1314.
- 16 J. B. Philipp, P. Majewski, L. Alff, A. Erb, R. Gross, T. Graf, D. D. Sarma, *et al.*, *Phys. Rev. B: Condens. Matter Mater. Phys.*, 2003, **68**(14), 144431.
- 17 A. Kumar, M. Kumar and R. P. Singh, *J. Mater. Sci.: Mater. Electron.*, 2021, **32**, 12951–12965.
- 18 S. A. Mir and D. C. Gupta, *J. Alloys Compd.*, 2021, **854**, 156000.
- 19 A. Harbi and M. Moutaabbid, *J. Supercond. Nov. Magnetism*, 2022, **35**(11), 3447–3456.
- 20 E. Haque, and M. A. Hossain, *arXiv*, 2018, preprint, arXiv:1802.08136, DOI: [10.48550/arXiv.1802.08136](https://doi.org/10.48550/arXiv.1802.08136).
- 21 U. Hira, J. W. G. Bos, S. S. Ali and F. Sher, *J. Alloys Compd.*, 2024, **984**, 173981.
- 22 D. Abdullah and D. C. Gupta, *Sci. Rep.*, 2023, **13**(1), 12795.
- 23 Y. Q. Zheng, J. Nuss and H. V. Schnering, Crystal structure of dithallium hexachlorotungstate (IV), $\text{Tl}_2[\text{WCl}_6]$, *Z. fur Krist.-New Cryst. Struct.*, 1998, **213**(1–4), 500.
- 24 F. Mouhat and F. X. Coudert, *Phys. Rev. B: Condens. Matter Mater. Phys.*, 2014, **90**(22), 224104.
- 25 I. Alhayek and M. S. Gaith, *JJMIE*, 2010, **4**(1), 55–60.



- 26 H. H. Hegazy, G. M. Mustafa, A. Nawaz, N. A. Noor, A. Dahshan and I. Boukhris, *J. Mater. Res. Technol.*, 2022, **19**, 1271–1281.
- 27 Q. Long, X. Nie, S. L. Shang, J. Wang, Y. Du, Z. Jin and Z. K. Liu, *Comput. Mater. Sci.*, 2016, **121**, 167–173.
- 28 D. H. Wu, H. C. Wang, L. T. Wei, R. K. Pan and B. Y. Tang, *..*, 2014, **2(2)**, 165–174.
- 29 M. A. Ali, R. Ullah, S. Abdullah, M. A. Khan, G. Murtaza, A. Laref and N. A. Kattan, *J. Solid State Chem.*, 2021, **293**, 121823.
- 30 A. Mahmood, S. M. Ramay, W. Al-Masry, C. W. Dunnill and N. Y. Al-Garadi, *J. Mater. Res. Technol.*, 2020, **9(6)**, 16159–16166.
- 31 F. Máca, J. Kudrnovský, V. Drchal and G. Bouzerar, *Appl. Phys. Lett.*, 2008, **92**, 212503.
- 32 F. Semari, N. Baki, H. Khachai, A. Yakoubi, S. Mécabih, R. Khenata, A. Bouhemadou, *et al.*, *Acta Phys. Pol., A*, 2017, **132(4)**, 1242–1250.
- 33 T. H. Flemban, T. Zelai, Q. Mahmood, A. A. S. Devi, M. Sajjad, M. H. Alhossainy, M. A. Amin, *et al.*, *J. Alloys Compd.*, 2022, **894**, 162313.
- 34 G. A. Mersal, H. Alkhalidi, G. M. Mustafa, Q. Mahmood, A. Mera, S. Bouzgarrou, M. A. Amin, *et al.*, *J. Mater. Res. Technol.*, 2022, **18**, 2831–2841.
- 35 S. Y. Back, H. Cho, Y. K. Kim, S. Byeon, H. Jin, K. Koumoto and J. S. Rhyee, *AIP Adv.*, 2018, **8(11)**, 115227.
- 36 N. H. Alotaibi, *J. Phys. Chem. Solids*, 2022, **171**, 110984.
- 37 N. H. Alotaibi, G. M. Mustafa, N. A. Kattan, Q. Mahmood, H. Albalawi, M. Morsi, M. A. Amin, *et al.*, *J. Solid State Chem.*, 2022, **313**, 123353.
- 38 S. A. Khandy, I. Islam, K. Kaur, A. M. Ali and A. F. Abd El-Rehim, *Mater. Chem. Phys.*, 2023, **297**, 127293.
- 39 Q. Mahmood, M. Younas, M. G. B. Ashiq, S. M. Ramay, A. Mahmood and H. M. Ghaithan, *Int. J. Energy Res.*, 2021, **45(10)**, 14995–15004.

